Title: PET imaging of tumor glycolysis downstream of hexokinase through non-invasive measurement of pyruvate kinase M2

Authors:

Timothy H Witney[1†], Michelle L James[1,2†], Bin Shen[1], Edwin Chang[1], Christoph Pohling[1], Natasha Arksey[1], Aileen Hoehne [1*], Adam Shuhendler[1], Jun-Hyung Park[1], Deepika Bodapati[1], Judith Weber[1], Gayatri Gowrishankar[1], Jianghong Rao[1], Frederick T Chin[1] & Sanjiv Sam Gambhir[1,3*]

Affiliations:

[1]*Department of Radiology, Molecular Imaging Program at Stanford, Stanford University, Stanford, CA, 943065, USA*

[2]*Department of Neurology and Neurological Sciences, Stanford University, Stanford, CA, 943065, USA*

[3]*Department of Bioengineering, Department of Materials Science & Engineering, Bio-X, Stanford University, Stanford, CA, 943065, USA*

[*]*Present address: 3B Pharmaceuticals GmbH, Magnusstrasse 11, 12489 Berlin, Germany*

†These authors contributed equally to this work

***Corresponding Author**: Sanjiv Sam Gambhir. E-mail: sgambhir@stanford.edu

Abstract

Cancer cells reprogram their metabolism to meet increased biosynthetic demands, commensurate with elevated rates of replication. Pyruvate kinase M2 (PKM2) catalyzes the final and rate-limiting step in tumor glycolysis, controlling the balance between energy production and the synthesis of metabolic precursors. We report here the synthesis and evaluation of a positron emission tomography (PET) radiotracer, [^{11}C]DASA-23, that provides a direct non-invasive measure of PKM2 expression in preclinical models of glioblastoma multiforme (GBM). *In vivo*, orthotopic U87 and GBM39 patient-derived tumors were clearly delineated from the surrounding normal brain tissue by PET imaging, corresponding to exclusive tumor-associated PKM2 expression. In addition, systemic treatment of mice with the PKM2 activator, TEPP-46, resulted in complete abrogation of the PET signal in intracranial GBM39 tumors. Together, these data provide the basis for the clinical evaluation of imaging agents that target this important gatekeeper of tumor glycolysis.

Introduction

Tumors undergo metabolic reprogramming to support the synthesis of new macromolecules required for rapid cell division, which also provides a selective advantage for progression and protection from cell death (*1*). The concept of metabolic adaptation in tumors was first described by Otto Warburg in the 1920s after the discovery that cancer cells display increased rates of glucose utilization in comparison to normal tissue, even under aerobic conditions (*2*). We now know that the metabolic transformation of cancer cells encompasses multiple interconnecting metabolic networks (*3, 4*), with feedback loops and crosstalk acting to provide plasticity and help the cells survive the steep and localized nutrient and oxygen gradients present in the harsh tumor microenvironment (*5*).

Central to tumor metabolism is the glycolytic pathway, which sustains tumors through the generation of ATP and synthesis of intermediates for biosynthetic reactions. Pyruvate kinase (PK) catalyzes the final and rate-limiting reaction in glycolysis, converting phosphoenolpyruvate (PEP) to pyruvate by transferring the high-energy phosphate group to ADP to produce ATP. PK consists of four isoforms, of which the spliced variant, PKM2, is preferentially expressed in all cancers studied to-date, regardless of their tissue of origin (*6*). PKM2 is allosterically regulated by the stabilization of a highly active tetramer relative to monomeric/dimeric PKM2. The tetramer of PKM2 has a high affinity for PEP, favoring synthesis of ATP and pyruvate, whereas the monomer/dimer has reduced activity because of its low affinity for PEP at physiological concentrations (*7*). When PKM2 is in the monomeric/dimeric conformation, reduced glycolytic flux through to pyruvate results in the accumulation of precursors for the biosynthesis of amino acids, nucleic acids, and phospholipids, commensurate with the production of reducing power

through pentose phosphate pathway-derived NADPH (*8*). A dynamic equilibrium between the two states of PKM2 enables tumor cells to switch between anabolic and catabolic metabolism (Fig. 1). Alternative splicing of PKM2 is controlled by c-Myc and HIF-1 oncogenes (reviewed in (*9*)), with quaternary structure of PKM2 tightly regulated by the glycolytic intermediate fructose 1,6-bisphosphate (FBP) (*10*) and growth factor signaling (*11*). In recent years, PKM2 has been targeted for cancer therapy through the development of small molecule activators that promote tetramer formation (*12, 13*).

Given the importance of PKM2 in the regulation of tumor metabolism, we sought to noninvasively measure its expression through the development of a PKM2-specifc radiopharmaceutical. A class of *N,N*-diarylsulfonamides (DASA) was reported by Boxer *et al*. in 2010 as highly promising PKM2 activators (*12*), known to promote PKM2 tetramer formation through binding at the subunit interaction interface of the PKM2 dimer in an allosteric pocket distinct from the binding site of fructose 1,6-bisphosphate and to inhibit tumor growth *in vivo* (*14*). Here we report the synthesis and evaluation of a positron emission tomography (PET) radiotracer for dimeric PKM2, [^{11}C]DASA-23, based on this class of compounds (Fig. 2A). DASA-23 was selected as a suitable candidate for ^{11}C labeling because of its high potency as a PKM2 activator (maximum activating concentration, AC_{50} = 90 nM (*12*)), favorable selectivity for PKM2 compared to other pyruvate kinase isozymes (PKM1, PKR, and PKL (*12*)) through reversible binding, and the presence of a methoxy moiety, which allows ^{11}C radiolabeling without modifying its structure. This chemotype is known to activate the PKM2 isoform by decreasing the K_m for PEP whilst maintaining PKM2's affinity for ADP; akin to the action of FBP (*12*). We demonstrate the ability of [^{11}C]DASA-23 to detect tumor-specific PKM2 in subcutaneous and orthotopic mouse models of human glioma *in*

vivo. Finally, we confirm the *in vivo* specificity and selectivity of [^{11}C]DASA-23 for PKM2 through pharmacological challenge in mice bearing patient-derived orthotopic xenografts (PDX) treated with TEPP-46, a structurally distinct class of PKM2 activator.

Results

[^{11}C]DASA-23 is rapidly taken up by tumor cells.

PKM2-23 was labeled at its aromatic methoxy moiety with ^{11}C ($t_{1/2}$ = 20.4 min) from the corresponding nor-derivative of DASA-23 and the highly efficient methylation reagent [^{11}C]CH_3OTf (Fig. 2A), with a radiochemical yield of 2.4 ± 0.8%, >99% radiochemical purity, and a specific activity of 159.2 ± 94.3 GBq/μmol at the end of synthesis (EOS; n = 12). The identity of the radiochemistry precursor and cold standard was confirmed through mass spectrometry and nuclear magnetic resonance (NMR) spectroscopy, and the identity of the radiotracer ([^{11}C]DASA-23) was confirmed by high performance liquid chromatography (HPLC) via co-injection with cold standard (fig. S1, S2, and S3, respectively). In cell studies, addition of [^{11}C]DASA-23 resulted in rapid and extensive cellular uptake in both HeLa and U87 tumor cells, reaching 14.9 ± 2.0 % radioactivity/mg protein and 19.6 ± 2.0 % radioactivity/mg protein, respectively, by 30 min (Fig. 2B & C). Removal of exogenous radioactivity resulted in efflux of cell-associated activity, with ~40% of the initial intracellular radioactivity retained 30 min after removal of exogenous [^{11}C]DASA-23 for both cell lines (Fig. 2B & C).

Retention of [^{11}C]DASA-23 is closely correlated to PKM2 expression

To determine the specificity of [^{11}C]DASA-23 in cancer cells, we modulated PKM2 protein expression in culture through small inhibitory RNA (siRNA). HeLa cells were selected due to their relative ease of transfection. Knockdown of PKM2 was observed at 48 hours after addition of PKM2 siRNA (siPKM2), with nearly complete protein ablation detected by 72 hours (Fig. 3A). Extended incubation of cells in culture medium in the presence of scrambled, non-targeting siRNA (siCtrl) induced a temporal increase in PKM2 protein expression. Low levels of PKM1 were measured in naïve cells and 72 hours after transfection with either siPKM2 or siCtrl (Supplemental Fig. S4). Next, we compared cell uptake of [^{11}C]DASA-23 to protein concentrations of PKM2 after siRNA knockdown. A significant 16.5% reduction in [^{11}C]DASA-23 uptake was measured in siPKM2 cells *versus* those transfected with control siRNA just 24 hours after transfection (P = 0.011; n = 3). After 72 hours, [^{11}C]DASA-23 uptake in siPKM2 cells was reduced to 44.5% of siCtrl cells ($P < 0.001$; n = 3; Fig. 3B). [^{11}C]DASA-23 strongly correlated with PKM2 protein expression, determined from analysis of the same cell lysates (R^2 = 0.83; P = 0.005), albeit with some non-specific cell retention in cells with low PKM2 expression (Fig. 3C).

[^{11}C]DASA-23 shows favorable characteristics for in vivo tumor imaging

Given the favorable tumor cell retention and specificity of [^{11}C]DASA in culture, we established small animal [^{11}C]DASA-23-PET in a nude mouse model implanted with subcutaneous (s.c.) U87 human glioma xenografts. [^{11}C]DASA-23 radiotracer distribution was characterized by liver uptake and clearance through both renal and hepatobiliary routes, accompanied by good tumor accumulation (Fig. 4A). *Ex vivo* biodistribution studies corroborated the PET imaging data (Fig. 4B). Of note, low [^{11}C]DASA-23 radioactivity was present in the brain 60 min after injection, at 0.86 ± 0.09 % of the injected dose (ID)/g. At this time point, U87 tumor uptake was 1.78 ± 0.23

%ID/g (n = 4 animals), and the tumor-to-blood, -muscle, and -brain ratios were 1.1, 1.6, and 2.1, respectively. Additionally, [^{11}C]DASA-23 showed excellent stability in plasma *ex vivo*, with >96% of the parent compound remaining after 60 min (Fig. 4C).

Dynamic [^{11}C]DASA-23 PET imaging confirmed rapid liver and kidney uptake, followed by clearance through the bladder and small intestine (Fig. 4D & E). Rapid tumor uptake of [^{11}C]DASA-23, peaking at 10 minutes, preceded a slow washout of radioactivity over the remaining 50 minutes (Fig. 4F). Muscle uptake of [^{11}C]DASA-23 followed a similar pattern of retention but at lower levels. This was contrasted with [^{11}C]DASA-23 uptake in the brain, where high initial delivery, peaking 30 s after injection (13.4 ± 1.9 %ID/g), was followed by rapid clearance, reaching low steady-state levels (2.3 ± 0.2 %ID/g) by 10 min after injection.

[^{11}C]DASA-23 accumulates in orthotopically-growing U87 tumors

We next explored the ability of [^{11}C]DASA-23 to image orthotopically grown U87 tumors. MicroPET after *i.v.* injection of [^{11}C]DASA-23 clearly allowed the detection of intracerebral tumors, shown in the fused PET-CT images (Fig. 5A; the corresponding 3D movie is displayed as movie S1, with a non-tumor-bearing mouse shown in movie S2 for comparison). Similarly to s.c. xenograft tumors, U87 tumor kinetics were characterized by rapid initial uptake preceding slow washout. In comparison, radioactivity from the control, contralateral, region of the brain reached similar levels of radiotracer delivery (P > 0.05; fig. S5), but it was not retained (Fig. 5B). Time course images of initial [^{11}C]DASA-23 uptake in the healthy brain and subsequent retention in orthotopic U87 tumors are shown in fig. S6. By 30 min after injection, [^{11}C]DASA-23 radioactivity in the tumor was 1.68 ± 0.47 %ID/g *versus* 0.78 ± 0.18 %ID/g in the contralateral background

tissue ($n = 6$; $P = 0.003$). To confirm that the PET signal corresponded with orthotopically-growing tumors, we performed contrast-enhanced MRI on the same animals (Fig. 5C) and co-registered these with the [^{11}C]DASA-23-PET images (Fig. 5D). Contrast-enhancing U87 tumors, clearly defined in the T_1-weighted images, excellently matched the corresponding microPET images. It is important to note that the trace amount of [^{11}C]DASA-23 (~200 pmol) used here was ~15,000× lower than the amount used in previous drug studies (~3 μmol) (*14*).

After imaging, the brains of tumor-bearing mice were excised for analysis by histopathology. H&E staining confirmed excellent correlation of PET signal intensity with histopathological findings (Fig 5E). The PET signal of orthotopic U87 tumors was sharply delineated from the surrounding brain tissue (Fig. 5D), matching the pattern of cytosolic PKM2 expression shown in tissue sections (Fig. 5E and fig. S7). PKM1 expression was exclusively located in the normal healthy brain and absent from intracranial tumors (Fig. 5E). At higher magnifications (10×; Fig. 5E *insert*), U87 tumor cells infiltrating away from the margins of the primary tumor were clearly delineated through the presence of PKM2 and absence of PKM1. Localization of [^{11}C]DASA-23 to small (~1 mm diameter) intracranial PKM2-positive tumors was shown through *ex vivo* autoradiography (fig. S8). Together, these data highlight the ability for [^{11}C]DASA-23-PET to clearly detect orthotopically growing human gliomas through measurement of tumor-specific PKM2 expression.

[^{11}C]DASA-23 shows utility as a PKM2 companion diagnostic in patient-derived intracranial tumors

Patient-derived xenograft (PDX) models are enhanced preclinical tools that better represent human tumor biology and patient response to therapy (*15*). To test whether [^{11}C]DASA-23-PET could

image these more clinically relevant tumors, we implanted GBM39 PDXs orthotopically in the brains of nude mice and monitored their growth via bioluminescence imaging (BLI). By 50 days after implantation, a strong BLI signal originating from the head of GBM39 tumor-bearing mice was evident (Fig. 6A). Mice were subsequently imaged with [^{11}C]DASA-23, which clearly identified the intracerebral tumors (Fig. 6B), appearing as distinct regions of infiltrative growth (Fig. 6C and movie S3).

Having previously demonstrated the specificity of [^{11}C]DASA-23 for the detection of PKM2 in cell culture (Fig. 3), we determined whether the PET signal originating from the intracranial tumors *in vivo* corresponded to tumor-specific PKM2 expression. The short half-life of carbon-11 permitted the use of the same mice in longitudinal studies, where [^{11}C]DASA-23 tumor uptake was assessed at baseline and subsequently after challenge with a blocking agent, 24 hours after initial evaluation. A structurally distinct PKM2 activator, TEPP-46, a highly selective PKM2 activator which binds with nM affinity (*16*), was selected to test the specificity of [^{11}C]DASA-23 for PKM2. One hour after TEPP-46 injection, animals were reimaged with [^{11}C]DASA-23, which revealed complete ablation of tumor signal to background levels present in the healthy contralateral regions of the brain (Fig. 6B & C and movie S4). This was expected because DASA-23 and TEPP-46 share the same PKM2 binding pocket, with TEPP-46-bound PKM2 made inaccessible for [^{11}C]DASA-23 binding and retention in tissues. Of interest was the reduction of retention of [^{11}C]DASA-23 in the harderian glands (Fig. 6C and movie S4), likely indicating PKM2 expression in this tissue. Contrast-enhanced MRI performed at the end of the study confirmed the presence of enhancing infiltrative tumors (Fig. 6D), with tumor-associated [^{11}C]DASA-23 retention 30 min after radiotracer injection reduced from 1.61 ± 0.25 % ID/g at baseline to 0.93 ± 0.10 % ID/g after

TEPP-46, a 42% decrease ($P = 0.0009$; $n = 7$; Fig. 6E). The uptake in control, contralateral healthy brain was 0.79 ± 0.18 % ID/g ($P = 0.10$). As with U87 tumors, autoradiography of excised GBM39-containing brains revealed precise localization of radioactivity to small PKM2-expressing tumors (figure 8D-F).

Discussion

Tumor cells reprogram their metabolism in response to the increased anabolic and catabolic demands of highly proliferative cells. For many metabolic pathways, the balance between biomolecular synthesis and energy production is highly regulated. An elegant example is the case of acetyl CoA carboxylase, which controls the opposing rates of fatty acid synthesis and β-oxidation on the basis of intracellular concentrations of acetyl CoA and malonyl CoA (*17*). Altered tumor glycolysis is mediated, in part, by PKM2 through transcriptional and epigenetic means (*18-20*), with a growing body of evidence demonstrating a critical role of PKM2 in tumorigenesis and progression (*6*). Further evidence suggests that PKM2 might provide a similar regulatory switch to acetyl CoA carboxylase: controlling the balance between glycolytically-derived anabolic and catabolic metabolism (*8, 11, 21, 22*). PKM2 has also been shown to translocate to the nucleus, where it functions to promote cell proliferation through interaction with HIF, STAT 3, Oct 4, and β-catenin (reviewed in (*9*)).

Clinically relevant imaging agents and modalities for the direct, non-invasive imaging of PKM2 are a topic of great interest and importance. PKM2 is overexpressed in tumors (*6*) and expressed in most tissues to varying degrees, with the exception of adult muscle, brain, and liver (*23-25*).

Given the intrinsically low background of PKM2 in the brain, we asked whether PKM2 is upregulated in transformed human glioblastoma cells, evaluated in orthotopic mouse models of the disease, and whether we could measure this transformation noninvasively through imaging. We developed a PET radiotracer for PKM2 by labeling a PKM2 activator, DASA-23, with carbon-11. DASA-23 has been shown to display selective activation of PKM2 (AC_{50} = 90 nM) *versus* other pyruvate kinase isozymes, PKM1, PKR, and PKL (*12*). Carbon-11 was selected for radiolabelling DASA-23 to retain its structure and therefore PKM2-binding selectivity.

In the present study, high [^{11}C]DASA-23 tumor cell uptake was measured in culture, with uptake strongly correlated to PKM2 protein expression. Nevertheless, we observed modest non-specific binding of [^{11}C]DASA-23 to cells with low PKM2 expression, which could reduce tumor-to-background contrast in living subjects. Because DASA-based activators are known to reversibly bind to dimeric PKM2 (*14*), efflux of the radiotracer from tumor cells after removal of exogenous activity was expected, although this occurred at a relatively slow rate. Of note was the ability of [^{11}C]DASA-23 to measure increased PKM2 expression in cells after prolonged incubation without the replacement of fresh medium (up to 72 hours). Cell adaptation to a reduced nutrient environment, akin to poorly perfused tumors *in vivo*, hints at an important role for PKM2 in the maintenance of metabolic homeostasis. When glucose is abundant, PKM2 is degraded via acetylation and chaperone-mediated autophagy, a process which is inhibited under nutrient stress (*20*). The ability to detect chronically nutrient-deprived cells through PKM2 imaging, may provide insights into tumor progression and metastasis, given that these cells are relatively chemoresistant (*5*).

Given the promising *in vitro* uptake profile and relatively high lipophilicity (cLogP = 3.4, ChemDraw Bio 13.0) of [^{11}C]DASA-23, required for diffusion across the blood brain barrier, we explored [^{11}C]DASA-23 for the preclinical *in vivo* imaging of human glioma. [^{11}C]DASA-23 could clearly image s.c. U87 tumor xenografts. The combined renal and hepatobiliary excretion profile for [^{11}C]DASA-23, however, may limit the imaging of PKM2 to tumors of the brain and upper thoracic region. Tumor-to-muscle and blood background ratios, although statistically significant, were below those typically observed with FDG-PET (*26*), which may further limit the assessment of PKM2 status to tumors of the brain and other tissues. We obtained PET/MR images of orthotopically-grown U87 gliomas, with [^{11}C]DASA-23 retention limited to tumor tissue. Low background radioactivity was detected in the brain after rapid initial uptake and washout, as predicted by the absence of PKM2 expression in this tissue (*25*), which was confirmed by our immunohistochemistry results. Indeed, PKM2 expression was exclusively confined to the intracranial tumor, which lacked PKM1. Autoradiographic analysis of tumor sections after saline perfusion, which removed un-bound/intravascular radioactivity from the brain, further confirmed tumor-specific binding of [^{11}C]DASA-23.

The increased glucose utilization of tumors in comparison to normal tissue (the "Warburg effect") has previously been exploited clinically to detect tumors and their response to treatment by [^{18}F]2-fluoro-2-deoxy-D-glucose ([^{18}F]FDG) PET. ^{18}F-FDG-PET is approved for use for the diagnosis of the majority of cancers (*27*), with particular utility for detecting metastases and nodal disease that appear normal on x-ray computed tomography scans (*28*). However, a high background uptake by surrounding normal tissue can mask tumor uptake, for example, in the brain (*29*). Thus, [^{11}C]DASA-23 has the potential to play an important role in the noninvasive measurement of

malignancies where FDG fails. Several other radiotracers, such as 3,4-dihydroxy-6-[^{18}F]fluoro-phenylalanine ([^{18}]F-FDOPA) (*30*), O-(2-[^{18}F]fluoroethyl)-L-tyrosine (FET) (*31*), 4-[^{18}F]-(2*S*,4*R*)-fluoroglutamine (*32*), and (4*S*)-4-(3-[^{18}F]fluoropropyl)-L-glutamate ([^{18}F]FSPG) (*33*), have shown great value for imaging tumors of the brain. The primary aim of our study, however, was to non-invasively measure PKM2 status in these tumors. Given the great interest in targeting PKM2 for cancer therapy (*12, 14, 34, 35*), we additionally explored the ability of [^{11}C]DASA-23 to report on the binding efficacy of these agents using orthotopically implanted PDX models of GBM. In these longitudinal studies, infiltrative GBM39 tumors were clearly delineated by PET, with tumor-specific retention of [^{11}C]DASA-23 abolished after pretreatment of the same animals with a bolus of TEPP-46, a structurally distinct class of PKM2 activators known to bind the same allosteric site as the DASA-class of activators (*14*). These data provide further evidence of the *in vivo* specificity of [^{11}C]DASA-23 for reporting on tumor-specific PKM2 expression and a potential role for both drug screening and the evaluation of precision medicine strategies. Furthermore, the observation that temozolomide-treated glioblastomas have reduced PKM2 expression (*36*) indicates that [^{11}C]DASA-23 may also provide a means to measure the efficacy of more traditional therapeutics.

In conclusion, we have synthesized and evaluated an imaging agent for the measurement of dimeric PKM2, [^{11}C]DASA-23. Through this work we showed that [^{11}C]DASA-23 enables the preclinical detection of orthotopically-growing human glioblastoma with aberrantly expressed PKM2. This study sets the foundation for the clinical translation of [^{11}C]DASA-23 for the imaging of primary brain tumors and potentially also other tumors that metastasize to the brain. In addition, our study confirms that [^{11}C]DASA-23 PET may be useful as a companion diagnostic to aid the development of the next generation of PKM2 activators.

Materials and methods

Study Design

The primary research objective was to design and synthesize an imaging agent to noninvasively measure tumor-specific pyruvate-kinase M2 (PKM2) in living subjects via PET. 6-7 animals per group were used for the evaluation of PKM2 in orthotopic models of GBM, calculated with 90% power and a 5% significance level. For TEPP-46 treatment studies, animals were randomized before imaging and subsequent treatment. All outliers were included in the analysis and no data were excluded. Authors were not blinded to the results. A minimum of 3 experimental replicates were recorded for all *in vitro* data.

Cell culture

HeLa cells (ATCC) and U87 human glioma cells (ATCC) were grown in Dulbecco modified Eagle medium (DMEM; Life Technologies), containing 10% FBS, 2 mM L-glutamine and 2.5 mL penicillin/streptomycin (100 $IU.mL^{-1}$/100 $mg.mL^{-1}$). GBM39, transfected with a lentiviral vector that expressed a fusion protein of GFP and firefly luciferase, was received as a gift from Dr. Paul Mischel (Ludwig Institute for Cancer Research, University of California, San Diego). GBM39 cells were grown in a defined, serum-free medium consisting of a 1:1 mixture of Neurobasal-A Medium DMEM/F12 that also contained HEPES Buffer Solution (10 mM), MEM sodium pyruvate solution (1 mM), MEM non-essential amino acids solution 10 mM (1×), GlutaMAX-I Supplement (1×), and antibiotic-antimycotic (1×) from Life Technologies Inc. The full working medium was additionally supplemented with H-EGF (20 ng/mL), H-FGF-basic-154 (20 ng/mL), H-PDGF-AA (10 ng/mL), H-PDGF-BB (10 ng/mL), and heparin solution, 0.2% (2 µg/mL) as

growth factors (all from Shenandoah Inc.) and B-27 (Life Technologies Inc). All cells were propagated at 37°C in a humidified atmosphere containing 5% CO_2.

Precursor and cold standard synthesis

The precursor for radiosynthesis was obtained through the reaction scheme illustrated in Figure 2A. 1-*tert*-butyloxycarbonyl(BOC)-piperazine **1** (1.34 mmol, 1 equiv.) was dissolved in dichloromethane (2.5 mL) under nitrogen and cooled to 0 °C. Triethylamine (2.68 mmol, 2.0 equiv.) was added followed by portion-wise addition of 2,6-difluorobenzenesulfonyl chloride **2** (1.48 mmol, 1.1 equiv.). The reaction was stirred at 0 °C for one hour and quenched with saturated aqueous ammonium chloride solution. The organic layer was washed with brine, dried over sodium sulfate, and concentrated *in vacuo*. The residue was purified via silica gel chromatography using a 95/5-5/95, hexane/EtOAc (*v/v*) gradient to give *tert*-butyl 4-((2,6 difluoro-phenyl)-sulfonyl)piperazine-1-carboxylate **3** as white crystals (80% yield).

BOC protected compound **3** (1.04 mmol) was dissolved in dichloromethane (1 mL) and cooled to 0°C. Trifluoroacetic acid (TFA, 1 mL) was added, and the reaction was monitored by TLC. After the reaction was complete, the solvents were evaporated *in vacuo* to yield the TFA salt of compound **4** as a light yellow oil, which was carried onto the next step without further purification. The oily residue **4** was dissolved in dichloromethane (2 mL) and cooled to 0°C. Triethylamine (4.16 mmol, 4 equiv.) was added followed by portion-wise addition of 4-hydroxybenzene-1-sulfonyl chloride (1.14 mmol, 1.1 equiv.). The progress of the reaction was monitored via TLC, and once complete, the reaction was quenched with saturated aqueous ammonium chloride solution (3 mL). The organic layer was washed twice with saturated ammonium chloride solution,

once with brine, dried over sodium sulfate, and concentrated *in vacuo*. The resulting product was dissolved in DMSO and purified by RP-HPLC [Phenomenex Luna C18 column (5 µm, 10 x 250 mm), water/acetonitrile gradient (70:30 - 10:90 in 30 min) containing 0.1% TFA (*v/v*); the extinction at 240 nm was monitored for detection], to yield the pure phenolic precursor as white crystals (33% yield). NMR spectra were acquired on a Varian Inova spectrometer operating at 300 MHz for ^{1}H and are referenced internally according to residual solvent signals. Data for ^{1}H NMR were recorded as follows: chemical shift (δ, ppm), multiplicity (s, singlet; d, doublet; t, triplet; m, multiplet; bs, broad singlet), integration, coupling constant (Hz). High-resolution mass spectra were obtained from the Vincent Coates Foundation Mass Spectrometry Laboratory at Stanford University. ^{1}H NMR ($CDCl_3$, 300 MHz): δ (ppm) = 7.661 (d, $^{3}J_{H,H}$ = 8.7 Hz, 2H), 7.574 (m, 1H), 7.075 (m, 2H), 6.987 (d, $^{3}J_{H,H}$ = 8.7 Hz, 2H), 5.648 (bs, 1H), 3.393 (m, 4H), 3.150 (m, 4H). MS (CI) ***m/z:*** $[M+H]^+$ calculated for $C_{16}H_{16}F_2N_2O_5S_2$ 419.05; found 419.08 (fig. S1).

DASA-23 was synthesized as a standard to confirm the identity of [^{11}C]DASA-23 using previously described methods (*12*). ^{1}H NMR ($CDCl_3$, 300 MHz): δ (ppm) = 7.685 (d, $^{3}J_{H,H}$ = 9.4 Hz, 2H), 7.563 (m, 1H), 7.057 (m, 4H), 3.921 (s, 3H), 3.392 (m, 4H), 3.151 (m, 4H) (fig. S2).

Radiosynthesis

Synthesis of [^{11}C]DASA-23 (Fig. 2A) was accomplished with a GE TRACERLab $FX_{C\ Pro}$ module by reacting 4-((4-((2,6-difluorophenyl)sulfonyl)piperazin-1-yl)sulfonyl)phenol (2.4 µmol) with [^{11}C]methyl triflate in acetonitrile (300 µL) for 3 min at 80 °C, using 5 N NaOH (24 µmol) as base. The reaction mixture was diluted with 1 mL water and loaded on a semi-prep HPLC for purification (Phenomenex Luna C18 5 µ, 250 x 10 mm, 50% acetonitrile, 50% 0.1 M NH_4HCO_2

with 0.5 % AcOH; 7 mL/min). The fraction corresponding to [^{11}C]DASA-23 (retention time, t_R = 9.5 min) was collected into a round flask preloaded with 20 mL water. The diluted aqueous fraction was passed through a pre-conditioned C-18 light Sep-Pak cartridge (Waters). The loaded cartridge was washed with sterile water (5 mL). [^{11}C]DASA-23 was eluted from the cartridge using ethanol (0.75 mL) and then saline (6.75 mL). The overall synthesis time was 52 min. Analytical HPLC (Phenomenex Gemini C18 5 µ, 250 x 4.6 mm, 60% acetonitrile, 40% 0.1 M NH_4HCO_2 with 0.5 % AcOH, 1 mL/min) was used for assessment of radiochemical purity and specific activity.

Cell uptake and efflux studies

U87 and HeLa cells (2×10^5) were plated into 6-well plates overnight before [^{11}C]DASA-23 uptake analysis. On the day of the experiment, fresh, pre-warmed DMEM containing 0.925 MBq of [^{11}C]DASA-23 was added to individual wells (1 mL/well; 9.25 ± 4.63 pmol). Cells were incubated with [^{11}C]DASA-23 at 37 °C and 5% CO_2 over a 60 min time course. At the indicated time points, plates were placed on ice, washed 3 times with ice-cold phosphate-buffered saline (PBS), and lysed in radio-immunoprecipitation assay buffer (Thermo Fisher Scientific Inc.; 500 µL). 300 µL cell lysates were transferred to counting tubes, and decay-corrected radioactivity was determined on a γ counter (Cobra II Auto-Gamma counter; Packard Biosciences Co.). The remaining lysate was frozen and used after radioactive decay for protein determination with a bicinchoninic acid (BCA) 96-well plate assay (Thermo Fisher Scientific Inc.) and for immunoblotting. In addition, 10 µL standards from the 0.925 MBq/mL solution added to cells were counted to quantitate percentage radiotracer uptake. For efflux studies, cells were incubated with radiotracer for 60 min and washed 3 times with room temperature (RT) Hank's Buffered Salt

Solution (HBSS) before subsequent incubation at 37 °C in fresh, radiotracer-free, DMEM. At the specified times, samples were processed as described above.

PKM2 siRNA

PKM2 knockdown in HeLa cells was performed over a time course of 72 hours after transfection. Cells were seeded in 6-well plates in antibiotic-free DMEM at 1.5×10^6 cells/well 24 hours before siRNA transfection with DharmaFECT1 (Thermo Scientific), according to the manufacturer's instructions. Specific siRNA targeting only PKM2 were custom made by Thermo Scientific using the following sequences: CCAUAAUCGUCCUCACCAAUU (sense), UUGGUGAGGACGAUUAUGGUU (antisense) (*37*). Scrambled siRNA (siCtrl; Cell Signaling Technology) was used as a control. siRNA were added at a final concentration of 25 nM. [^{11}C]DASA-23 uptake (0.925 MBq/mL) was measured after 30 min in cells transfected with siCtrl and siPKM2 at 24, 48, and 72 hours after transfection, after being processed as described in '*Cell uptake and efflux studies'*. Untreated cells were used as a further control, measured 24 hours after addition of fresh DMEM and 96 hours after seeding.

Western blotting

Monoclonal rabbit antibodies to PKM1 and PKM2 (1:1000 dilution, Cell Signaling Technology) were used in a standard western blotting protocol. A rabbit anti-actin antibody (Sigma-Aldrich Co. Ltd; 1:2000) was used as a loading control. Blots were scanned and signal was quantified with ImageJ (National Institutes of Health).

In vivo tumor models

All experimental procedures involving animals were approved by Stanford University Institutional Animal Care and Use Committee. For s.c. tumor models, U87 tumor cells (5×10^6 cells; 100 µL PBS) were injected subcutaneously on the back of female BALB/c nude mice (aged 6 – 8 weeks; Charles River Laboratories) and grown to ~150 mm^3. Tumor dimensions were measured periodically using a caliper (by the same researcher), with tumor volumes calculated by the equation: volume = $(\pi / 6) \times a \times b \times c$, where *a*, *b*, and *c* represent three orthogonal axes of the tumor. For orthotopic brain tumor models, either 2×10^5 U87 or 4×10^5 GBM39 cells were implanted in the right hemisphere, 0.5 mm anterior and 2 mm lateral to the lambda, in the brains of 6 – 8 week-old nude mice held in place with a stereotaxic unit (Stoelting). The cells, suspended in 4 µL PBS, were injected at a depth of 3 mm over 5 min with an AS blunt-ended Hamilton syringe, which was subsequently held in place for a further 5 min. Animals were anesthetized with an i.p. injection of 150 mg/kg ketamine, 15 mg/kg xylazine. U87 tumor-bearing mice were subsequently imaged by MRI and PET 32-35 days after intracranial injection, and GBM39 tumor-bearing mice were imaged between 44-50 days after implantation. For blocking studies, mice were imaged with [^{11}C]DASA-23 at baseline and then 24 hours later with a second tail-vein injection of [^{11}C]DASA-23, 1 hour after i.p. injection of TEPP-46 [50 mg/kg in 40% *w/v* (2-hydroxypropyl)-β-cyclodextrin in water; ~3 µmol; Cayman Chemical].

Imaging studies

MRI was performed at the Stanford Clark Center Small Animal Imaging Facility in an actively-shielded Discovery MR901 General Electric 7T horizontal bore scanner (GE Healthcare) including Integrated Electronics Company (IECO) gradient drivers, an Agilent 120 mm inner

diameter shielded gradient insert (600 mT/m, 1000 T/m/s), EXCITE2 electronics, the supporting LX11 platform, and a 3 cm inner diameter Millipede quadrature transmit/receive volume RF coil. Animals were anesthetized with 2% isoflurane in oxygen, and physiological monitoring included respiration and temperature feedback for maintaining surface body temperature by warm airflow over the animal. A fast spoiled gradient echo (FSPGR) sequence (TR = 9.7 ms; TE = 2.1 ms; flip angle = 5°; NEX = 20; FOV = 2 cm; image matrix = 160 × 160; slice thickness = 1 mm) was used to acquire 3 sets of 12, 12, and 8 orthogonal T_1-weighted images in the axial, sagittal, and coronal planes through the mass, respectively. PET-MR registration was performed in IRW (Siemens) using the CT image for alignment of the skull.

PET imaging scans were carried out on a docked Siemens Inveon PET/CT scanner (matrix size, 128 × 128 × 159; CT attenuation-corrected; non-scatter corrected), after a bolus *i.v.* injection of ~18.5 MBq of [^{11}C]DASA-23 into tumor-bearing mice (185 ± 92.5 pmol). Dynamic scans were acquired in list mode format over 60 min. The acquired data were then sorted into 0.5-mm sinogram bins and 19 time frames for image reconstruction (4 × 15 s, 4 × 60 s, and 11 × 300 s), which was done by iterative reconstruction with the following parameters: 3D ordered-subsets expectation maximization (3D-OSEM) followed by fast maximum a posteriori (fastMAP); MAP OSEM iterations, 2; MAP subsets, 16; MAP iterations, 18. The count densities were averaged for all volumes of interest at each time point to obtain a time versus radioactivity curve (TAC). Tumor and tissue TACs were normalized to injected dose, measured by a CRC-15 PET dose calibrator (Capintec, Inc.), and expressed as percentage injected dose per gram of tissue (%ID/g), assuming 1 g/mL. The normalized uptake of radiotracer at 30 min (%ID/g_{30}) was also used for comparison. Siemens Inveon Research Workplace software (v.4.0) was used for visualization of radiotracer

uptake in the tumor, to define the three-dimensional (3D) volumes of interest (VOI) and for 3D visualisation to create volume rendering technique (VRT) images.

Ex vivo biodistribution

After the PET imaging studies, 60 min after radiotracer administration, mice were sacrificed by exsanguination via cardiac puncture and tissues were harvested. Tissue radioactivity for all organs was subsequently determined on a gamma counter (decay-corrected; Cobra II Auto-Gamma counter, Packard Biosciences Co.). Ten-microliter standards from the stock activity were also counted for data normalization. Data were expressed as percent injected dose per gram of tissue (%ID/g).

Ex vivo autoradiography

Autoradiography was performed as in (*38*). In brief, coronal brain sections of U87 and GBM39 tumor-bearing mice were obtained 20 min after *i.v.* injection of 26 MBq [^{11}C]DASA-23. Anesthetized mice were perfused with saline (10 mL) to remove intravascular [^{11}C]DASA-23, and after cervical dislocation, the brain was removed and embedded in optimal cutting temperature (OCT) compound (Tissue-Tek) before being frozen on dry ice. Subsequently, 10 μm thick coronal brain sections were cut with a cryostat microtome HM500 (Microm). The sections were mounted on microscope slides (Fisherbrand Superfrost Plus microscope slides), air-dried for a minimum of 5 min, and then exposed to MultiSensitive storage phosphor screens (Perkin-Elmer) for 3 hours at -20 °C. The image plates were analyzed with a Typhoon 9410 variable mode imager (Amersham Biosciences), and image data were visualized and processed by Image J.

Plasma stability

[^{11}C]DASA-23 stability in mouse plasma was assessed *ex vivo* according to previously described methodology (*38*). Samples were incubated for 10, 30, and 60 min and compared to a standard from the respective injected radiotracer formulation.

Histopathology

After imaging, anesthetized mice bearing orthotopically-implanted U87 tumors were transcardially perfused with 0.9% saline, followed by the removal of the brain. Formalin-fixed brains (10% *v/v*) were embedded in paraffin, coronally sectioned into 5 µm-thick slices and mounted on microscope slides according to standard procedures (Histo-Tec laboratory). Sections were taken at regular intervals across the entire brain. Every sixth section was stained with hematoxylin and eosin (H&E; Histo-Tec laboratory). Immunohistochemistry against PKM1 and PKM2 was performed on paraffin-embedded sections with rabbit monoclonal antibodies reactive to both mouse and human isozymes (Cell Signaling Technology; 1:100) using standard techniques and according to the manufacturer's instructions (Cell Signaling Technology). Before staining, antigen retrieval was performed in 10 mM sodium citrate buffer at 90 °C for 10 min. For detection, VECTASTAIN Elite ABC and Vector NovaRED (Vector Laboratories) were used per manufacturer's recommendations. Histopathological staining (H&E and PKM2) of fresh-frozen sections taken for autoradiography was processed using standard techniques and according to the manufacturer's instructions (Cell Signaling Technology).

Statistical analysis

Data were expressed as mean ± SD. Statistical significance was determined using a two-tailed Student's *t* test. Paired *t* tests were used for longitudinal studies (Fig. 6E), with unpaired *t* tests used to derive significance for all other analyses. For the analysis of [^{11}C]DASA-23 uptake in multiple tissues, significance was determined by ANOVA, followed by Tukey's honest significant difference test. Correlation analysis using Spearman's rank correlation, linear regression, statistical significance, and 95% confidence levels were determined using Prism software for Mac OSX (v.6.0e; GraphPad Software). Differences between groups were considered significant if $P \leq 0.05$.

Supplementary Materials

References and notes

1. R. A. Cairns, I. S. Harris, T. W. Mak, Regulation of cancer cell metabolism. *Nat Rev Cancer* **11**, 85-95 (2011).
2. O. Warburg, On the origin of cancer cells. *Science* **123**, 309-314 (1956).
3. L. K. Boroughs, R. J. DeBerardinis, Metabolic pathways promoting cancer cell survival and growth. *Nat Cell Biol* **17**, 351-359 (2015).
4. A. Carracedo, L. C. Cantley, P. P. Pandolfi, Cancer metabolism: fatty acid oxidation in the limelight. *Nat Rev Cancer* **13**, 227-232 (2013).
5. R. A. Gatenby, R. J. Gillies, Why do cancers have high aerobic glycolysis? *Nat Rev Cancer* **4**, 891-899 (2004).
6. N. Wong, J. De Melo, D. Tang, PKM2, a Central Point of Regulation in Cancer Metabolism. *Int J Cell Biol* **2013**, 242513 (2013).
7. J. D. Dombrauckas, B. D. Santarsiero, A. D. Mesecar, Structural basis for tumor pyruvate kinase M2 allosteric regulation and catalysis. *Biochemistry* **44**, 9417-9429 (2005).
8. S. Mazurek, Pyruvate kinase type M2: a key regulator of the metabolic budget system in tumor cells. *Int J Biochem Cell Biol* **43**, 969-980 (2011).
9. B. Chaneton, E. Gottlieb, Rocking cell metabolism: revised functions of the key glycolytic regulator PKM2 in cancer. *Trends Biochem Sci* **37**, 309-316 (2012).
10. E. Bailey, F. Stirpe, C. B. Taylor, Regulation of rat liver pyruvate kinase. The effect of preincubation, pH, copper ions, fructose 1,6-diphosphate and dietary changes on enzyme activity. *Biochem J* **108**, 427-436 (1968).
11. H. R. Christofk, M. G. Vander Heiden, N. Wu, J. M. Asara, L. C. Cantley, Pyruvate kinase M2 is a phosphotyrosine-binding protein. *Nature* **452**, 181-186 (2008).

12. M. B. Boxer, J. K. Jiang, M. G. Vander Heiden, M. Shen, A. P. Skoumbourdis, N. Southall, H. Veith, W. Leister, C. P. Austin, H. W. Park, J. Inglese, L. C. Cantley, D. S. Auld, C. J. Thomas, Evaluation of substituted N,N'-diarylsulfonamides as activators of the tumor cell specific M2 isoform of pyruvate kinase. *J Med Chem* **53**, 1048-1055 (2010).

13. W. J. Israelsen, T. L. Dayton, S. M. Davidson, B. P. Fiske, A. M. Hosios, G. Bellinger, J. Li, Y. Yu, M. Sasaki, J. W. Horner, L. N. Burga, J. Xie, M. J. Jurczak, R. A. DePinho, C. B. Clish, T. Jacks, R. G. Kibbey, G. M. Wulf, D. Di Vizio, G. B. Mills, L. C. Cantley, M. G. Vander Heiden, PKM2 isoform-specific deletion reveals a differential requirement for pyruvate kinase in tumor cells. *Cell* **155**, 397-409 (2013).

14. D. Anastasiou, Y. Yu, W. J. Israelsen, J. K. Jiang, M. B. Boxer, B. S. Hong, W. Tempel, S. Dimov, M. Shen, A. Jha, H. Yang, K. R. Mattaini, C. M. Metallo, B. P. Fiske, K. D. Courtney, S. Malstrom, T. M. Khan, C. Kung, A. P. Skoumbourdis, H. Veith, N. Southall, M. J. Walsh, K. R. Brimacombe, W. Leister, S. Y. Lunt, Z. R. Johnson, K. E. Yen, K. Kunii, S. M. Davidson, H. R. Christofk, C. P. Austin, J. Inglese, M. H. Harris, J. M. Asara, G. Stephanopoulos, F. G. Salituro, S. Jin, L. Dang, D. S. Auld, H. W. Park, L. C. Cantley, C. J. Thomas, M. G. Vander Heiden, Pyruvate kinase M2 activators promote tetramer formation and suppress tumorigenesis. *Nat Chem Biol* **8**, 839-847 (2012).

15. M. Hidalgo, F. Amant, A. V. Biankin, E. Budinska, A. T. Byrne, C. Caldas, R. B. Clarke, S. de Jong, J. Jonkers, G. M. Maelandsmo, S. Roman-Roman, J. Seoane, L. Trusolino, A. Villanueva, Patient-derived xenograft models: an emerging platform for translational cancer research. *Cancer Discov* **4**, 998-1013 (2014).

16. J. K. Jiang, M. B. Boxer, M. G. Vander Heiden, M. Shen, A. P. Skoumbourdis, N. Southall, H. Veith, W. Leister, C. P. Austin, H. W. Park, J. Inglese, L. C. Cantley, D. S. Auld, C. J. Thomas, Evaluation of thieno[3,2-b]pyrrole[3,2-d]pyridazinones as activators of the tumor cell specific M2 isoform of pyruvate kinase. *Bioorg Med Chem Lett* **20**, 3387-3393 (2010).

17. L. Tong, Acetyl-coenzyme A carboxylase: crucial metabolic enzyme and attractive target for drug discovery. *Cell Mol Life Sci* **62**, 1784-1803 (2005).

18. C. J. David, M. Chen, M. Assanah, P. Canoll, J. L. Manley, HnRNP proteins controlled by c-Myc deregulate pyruvate kinase mRNA splicing in cancer. *Nature* **463**, 364-U114 (2010).

19. W. B. Luo, H. X. Hu, R. Chang, J. Zhong, M. Knabel, R. O'Meally, R. N. Cole, A. Pandey, G. L. Semenza, Pyruvate Kinase M2 Is a PHD3-Stimulated Coactivator for Hypoxia-Inducible Factor 1. *Cell* **145**, 732-744 (2011).

20. L. Lv, D. Li, D. Zhao, R. Lin, Y. Chu, H. Zhang, Z. Zha, Y. Liu, Z. Li, Y. Xu, G. Wang, Y. Huang, Y. Xiong, K. L. Guan, Q. Y. Lei, Acetylation targets the M2 isoform of pyruvate kinase for degradation through chaperone-mediated autophagy and promotes tumor growth. *Mol Cell* **42**, 719-730 (2011).

21. E. Eigenbrodt, M. Reinacher, U. Scheefers-Borchel, H. Scheefers, R. Friis, Double role for pyruvate kinase type M2 in the expansion of phosphometabolite pools found in tumor cells. *Crit Rev Oncog* **3**, 91-115 (1992).

22. M. G. Vander Heiden, L. C. Cantley, C. B. Thompson, Understanding the Warburg effect: the metabolic requirements of cell proliferation. *Science* **324**, 1029-1033 (2009).

23. K. Bluemlein, N. M. Gruning, R. G. Feichtinger, H. Lehrach, B. Kofler, M. Ralser, No evidence for a shift in pyruvate kinase PKM1 to PKM2 expression during tumorigenesis. *Oncotarget* **2**, 393-400 (2011).

24. H. R. Christofk, M. G. Vander Heiden, M. H. Harris, A. Ramanathan, R. E. Gerszten, R. Wei, M. D. Fleming, S. L. Schreiber, L. C. Cantley, The M2 splice isoform of pyruvate kinase is important for cancer metabolism and tumour growth. *Nature* **452**, 230-233 (2008).

25. K. Imamura, T. Tanaka, Multimolecular forms of pyruvate kinase from rat and other mammalian tissues. I. Electrophoretic studies. *J Biochem* **71**, 1043-1051 (1972).

26. T. H. Witney, A. Hoehne, R. E. Reeves, O. Ilovich, M. Namavari, B. Shen, F. T. Chin, J. Rao, S. S. Gambhir, A Systematic Comparison of 18F-C-SNAT to Established Radiotracer Imaging Agents for the Detection of Tumor Response to Treatment. *Clin Cancer Res*, **21**, 3896-3905 (2015).

27. G. J. Kelloff, J. M. Hoffman, B. Johnson, H. I. Scher, B. A. Siegel, E. Y. Cheng, B. D. Cheson, J. O'Shaughnessy, K. Z. Guyton, D. A. Mankoff, L. Shankar, S. M. Larson, C. C. Sigman, R. L. Schilsky, D. C. Sullivan, Progress and promise of FDG-PET imaging for cancer patient management and oncologic drug development. *Clin Cancer Res* **11**, 2785-2808 (2005).

28. A. Sharma, P. Fidias, L. A. Hayman, S. L. Loomis, K. H. Taber, S. L. Aquino, Patterns of lymphadenopathy in thoracic malignancies. *Radiographics* **24**, 419-434 (2004).

29. M. E. Phelps, J. C. Mazziotta, Positron emission tomography: human brain function and biochemistry. *Science* **228**, 799-809 (1985).

30. S. Karunanithi, P. Sharma, A. Kumar, B. C. Khangembam, G. P. Bandopadhyaya, R. Kumar, D. K. Gupta, A. Malhotra, C. Bal, 18F-FDOPA PET/CT for detection of recurrence in patients with glioma: prospective comparison with 18F-FDG PET/CT. *Eur J Nucl Med Mol Imaging* **40**, 1025-1035 (2013).

31. W. A. Weber, H. J. Wester, A. L. Grosu, M. Herz, B. Dzewas, H. J. Feldmann, M. Molls, G. Stocklin, M. Schwaiger, O-(2-[18F]fluoroethyl)-L-tyrosine and L-[methyl-11C]methionine uptake in brain tumours: initial results of a comparative study. *Eur J Nucl Med* **27**, 542-549 (2000).

32. S. Venneti, M. P. Dunphy, H. Zhang, K. L. Pitter, P. Zanzonico, C. Campos, S. D. Carlin, G. La Rocca, S. Lyashchenko, K. Ploessl, D. Rohle, A. M. Omuro, J. R. Cross, C. W. Brennan, W. A. Weber, E. C. Holland, I. K. Mellinghoff, H. F. Kung, J. S. Lewis, C. B. Thompson, Glutamine-based PET imaging facilitates enhanced metabolic evaluation of gliomas in vivo. *Sci Transl Med* **7**, 274ra217 (2015).

33. S. Baek, C. M. Choi, S. H. Ahn, J. W. Lee, G. Gong, J. S. Ryu, S. J. Oh, C. Bacher-Stier, L. Fels, N. Koglin, C. Hultsch, C. A. Schatz, L. M. Dinkelborg, E. S. Mittra, S. S. Gambhir, D. H. Moon, Exploratory clinical trial of (4S)-4-(3-[18F]fluoropropyl)-L-glutamate for imaging xC- transporter using positron emission tomography in patients with non-small cell lung or breast cancer. *Clin Cancer Res* **18**, 5427-5437 (2012).

34. M. G. Vander Heiden, H. R. Christofk, E. Schuman, A. O. Subtelny, H. Sharfi, E. E. Harlow, J. Xian, L. C. Cantley, Identification of small molecule inhibitors of pyruvate kinase M2. *Biochem Pharmacol* **79**, 1118-1124 (2010).

35. M. J. Walsh, K. R. Brimacombe, H. Veith, J. M. Bougie, T. Daniel, W. Leister, L. C. Cantley, W. J. Israelsen, M. G. Vander Heiden, M. Shen, D. S. Auld, C. J. Thomas, M. B.

Boxer, 2-Oxo-N-aryl-1,2,3,4-tetrahydroquinoline-6-sulfonamides as activators of the tumor cell specific M2 isoform of pyruvate kinase. *Bioorg Med Chem Lett* **21**, 6322-6327 (2011).

36. I. Park, J. Mukherjee, M. Ito, M. M. Chaumeil, L. E. Jalbert, K. Gaensler, S. M. Ronen, S. J. Nelson, R. O. Pieper, Changes in pyruvate metabolism detected by magnetic resonance imaging are linked to DNA damage and serve as a sensor of temozolomide response in glioblastoma cells. *Cancer Res* **74**, 7115-7124 (2014).
37. M. S. Goldberg, P. A. Sharp, Pyruvate kinase M2-specific siRNA induces apoptosis and tumor regression. *J Exp Med* **209**, 217-224 (2012).
38. M. L. James, B. Shen, C. L. Zavaleta, C. H. Nielsen, C. Mesangeau, P. K. Vuppala, C. Chan, B. A. Avery, J. A. Fishback, R. R. Matsumoto, S. S. Gambhir, C. R. McCurdy, F. T. Chin, New positron emission tomography (PET) radioligand for imaging sigma-1 receptors in living subjects. *J Med Chem* **55**, 8272-8282 (2012).

Acknowledgements: We thank Dr. Paul Mischel (Ludwig Institute for Cancer Research, University of California, San Diego) for providing GM39 tumor cells. We would also like to acknowledge use of the SCi3 Small Animal Imaging Service Center, which was used to acquire data presented in this study. Specifically, we would like to thank Dr. Laura Pisani for assistance with MRI acquisition.

Funding: This work was funded by the Ben and Catherine Ivy Foundation (S.S.G. and E.C.), the Canary Foundation (S.S.G.), and the NCI ICMIC P50 CA114747 (S.S.G). The SCi3 Small Animal Imaging Service Center is supported by NCI grants 1P50CA114747-10 (ICMIC P50) and CA124435-04 (Cancer Center P30).

Author contributions: The project was initially conceptualized by S.S.G. with the idea of developing a PET tracer for PKM2. The entire project was supervised by S.S.G. The study was designed by S.S.G., T.H.W. and M.L.J. Data acquisition was performed by T.H.W., M.L.J., B.S., E.C., C.P., N.A., A.H., A.S., J-H.P., D.B. and J.W. . T.H.W., M.L.J., B.S., E.C., C.P., A.H., A.S., J.R., F.C. and S.S.G. participated in the design and/or interpretation of the reported experiments or results. T.H.W. wrote the manuscript draft which was then further refined by S.S.G. All other authors reviewed and edited the intermediate and final versions of the manuscript.

Competing interests: The authors filed a provisional patent titled "Imaging tumor pyruvate kinase M2 (PKM2) expression by positron emission tomography."

Data and materials availability: Where possible, all materials and cell lines derived for this study will be made available upon request.

Figures

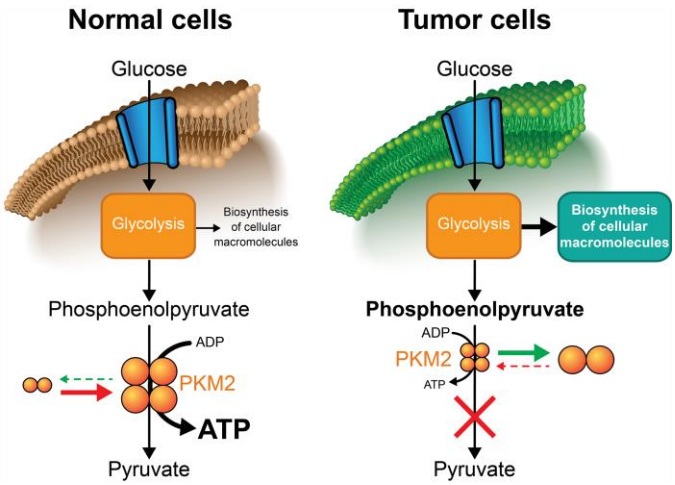

Fig. 1. Schematic illustrating the control of normal and tumor cell glycolysis by pyruvate kinase M2. Pyruvate kinase catalyzes the final step of glycolysis, resulting in net ATP synthesis through the dephosphorylation of phosphoenolpyruvate. The pyruvate kinase M2 (PKM2) isozyme predominates in proliferating non-tumor and tumor cells. Two quaternary PKM2 conformations exist as homo-dimeric or –tetrameric forms (shown above as two orange spheres and four orange spheres, respectively). Dimeric PKM2 has reduced affinity for phosphoenolpyruvate in comparison to the tetramer, with tumor PKM2 mainly present in the dimeric form. The reduced conversion of phosphoenolpyruvate to pyruvate results in a buildup of glycolytic precursors that can subsequently be used by alternative pathways for the biosynthesis of cellular macromolecules. Conversely, PKM2 is mostly present in the tetrameric form in non-tumor cells.

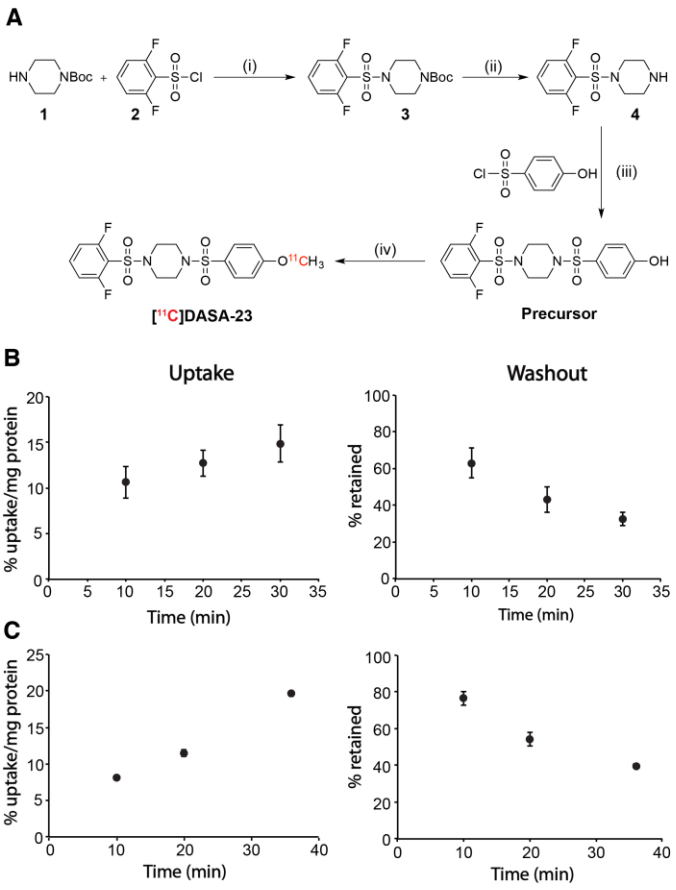

Fig. 2. Radiosynthesis, tumor cell uptake, retention, and washout of [^{11}C]DASA-23. (**A**). Synthesis of the precursor 4-((4-((2,6-difluorophenyl)sulfonyl)piperazin-1-yl)sulfonyl)phenol, and the ^{11}C-labeled compound [^{11}C]DASA-23 (1-((2,6-difluorophenyl)sulfon-yl)-4-((4-(methoxy-^{11}C)phenyl)sulfonyl)piperazine). Reagents and conditions: (i) dichloromethane, triethylamine, 0 °C, 1 h; (ii) dichloromethane, trifluoroacetic acid, 0 °C, 1 h; (iii) dichloromethane, triethylamine, 0 °C, 1 h; (iv) acetonitrile, [^{11}C]methyl triflate, NaOH, 80 °C, 3 min. The radioisotope is labeled in red. Cell uptake and washout of [^{11}C]DASA-23 was assessed in human HeLa cervical adenocarcinoma (**B**) and U87 glioma cells (**C**). Data shown as mean ± SD (n = 3).

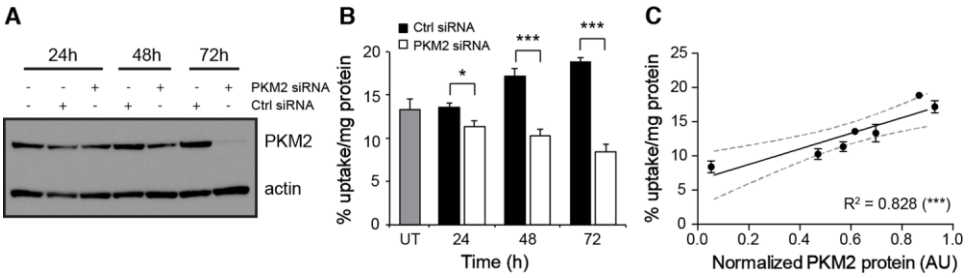

Fig. 3. Specificity of [^{11}C]DASA-23 for detecting PKM2 expression in cells. (**A**) Time course of PKM2 knockdown by siRNA in HeLa cells in comparison to scrambled siRNA and untreated control cells. Representative western blot from whole cell lysate is shown, with actin used as a loading control. (**B**) [^{11}C]DASA-23 cell uptake after perturbation of PKM2 expression. (**C**) Correlation between PKM2 protein expression and [^{11}C]DASA-23 uptake after PKM2 knockdown. 95% confidence levels are represented as dashed lines. Data shown as mean ± SD (*n* = 3). *, *P* = 0.011; ***, *P* = 0.0006, *P* = 0.0001, and *P* = 0.0045 for 24 h, 48 h, and 72 h siRNA treatment, and for the correlation between PKM2 protein and [^{11}C]DASA-23 uptake, respectively. Abbreviations: UT, untreated; Ctrl, control.

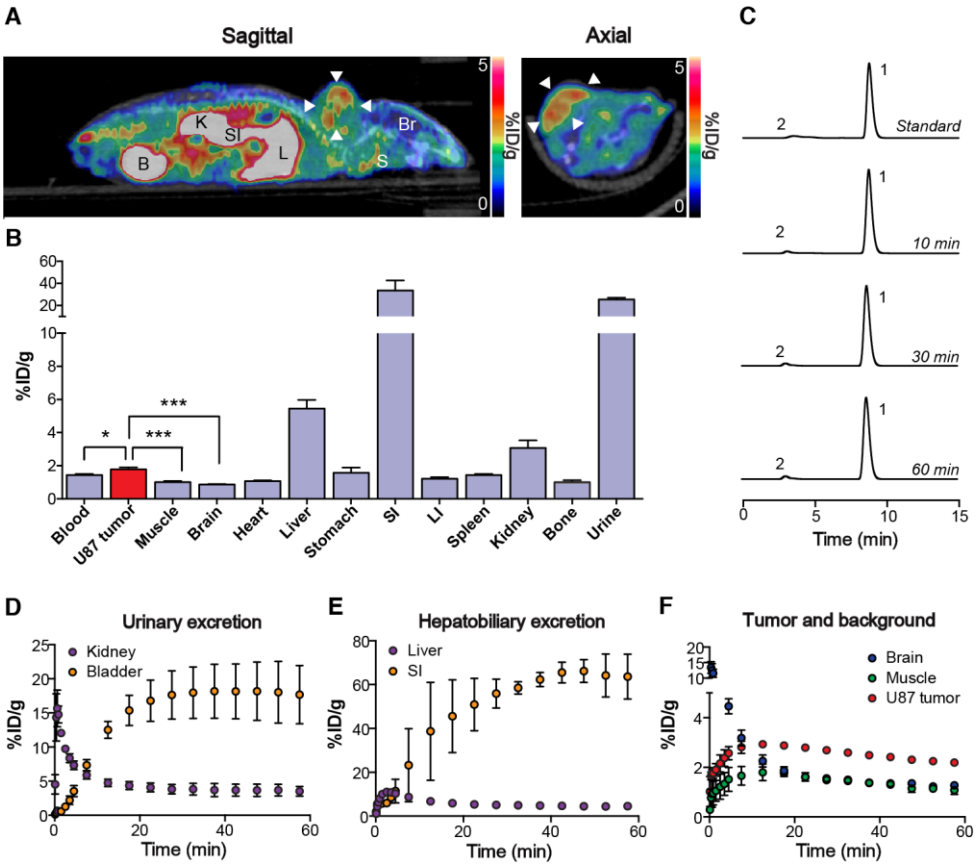

Fig. 4. PET/CT imaging, *ex vivo* biodistribution, and stability of [^{11}C]DASA-23 in mice bearing subcutaneous U87 glioblastoma xenografts. (**A**) Representative 30-60 min sagittal and axial fused PET/CT images. Nude mice received ~18.5 MBq of [^{11}C]DASA-23 via tail vein injection, with PET/CT images acquired 30-60 min after injection. Arrowheads indicate the tumor, identified from the CT image. (**B**) *Ex vivo* biodistribution at 60 min after injection. Data shown as mean ± SD (n = 6 animals). *, $P < 0.05$; ***, $P < 0.001$. (**C**) *Ex vivo* mouse serum stability of [^{11}C]DASA-23. [^{11}C]DASA-23 was incubated in mouse serum for the indicated amounts of time at 37 °C and compared to a [^{11}C]DASA-23 standard. *Peak 1*, [^{11}C]DASA-23; *Peak 2*, unknown metabolite. (**D**) Temporal urinary and (**E**) hepatobiliary excretion of [^{11}C]DASA-23 by dynamic PET. (**F**) The tumor TAC representing average counts from a dynamic 60-minute scan for U87 s.c. tumors compared to [^{11}C]DASA-23 uptake profiles for the muscle and normal brain. Data

shown as mean ± SD (n = 3 animals). Abbreviations: L, liver; S, salivary gland; SI, small intestine; K, kidney; B, bladder; Br, brain; LI, large intestine.

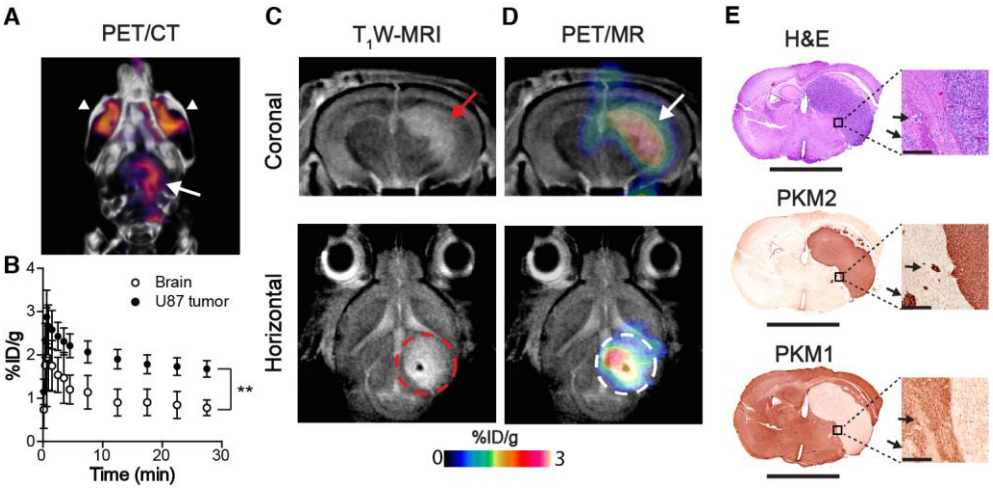

Fig. 5. Non-invasive imaging of mice bearing orthotopic U87 human gliomas. (**A**) Representative fused [^{11}C]DASA-23-PET/CT (10 – 30 min summed activity) 3D volume rendering technique (VRT) image of the head of a mouse containing an orthotopically-grown U87 tumor. Gray scale is CT image and color scale is PET image. The long white arrow indicates the tumor. [^{11}C]DASA-23 accumulation in the harderian glands is indicated by white arrow heads. (**B**) Orthotopic U87 tumor and corresponding contralateral normal brain TAC taken from dynamic [^{11}C]DASA-23-PET/CT images. Data shown as mean ± SD (n = 6 animals). **, $P < 0.01$. (**C**) Representative contrast-enhanced T_1-weighted MR coronal and horizontal images of orthotopically-implanted U87 gliomas. (**D**) Corresponding merged [^{11}C]DASA-23-PET/MR images (10 – 30 min summed [^{11}C]DASA-23 activity). Arrows and dashed circles indicate regions of contrast enhancement and radiotracer uptake, corresponding to the tumor. (**E)** Histopathological analysis of orthotopic U87 human gliomas. Whole brain sections were stained with H&E, PKM2, or PKM1 (scale bar = 5 mm). Higher magnification views of the boxed areas in the tumor periphery

are also displayed (10×; scale bar = 250 µm). Arrows indicate U87 tumor cells infiltrating away from the margins of the primary tumor. T_1W-MRI, T_1-weighted nuclear magnetic resonance imaging.

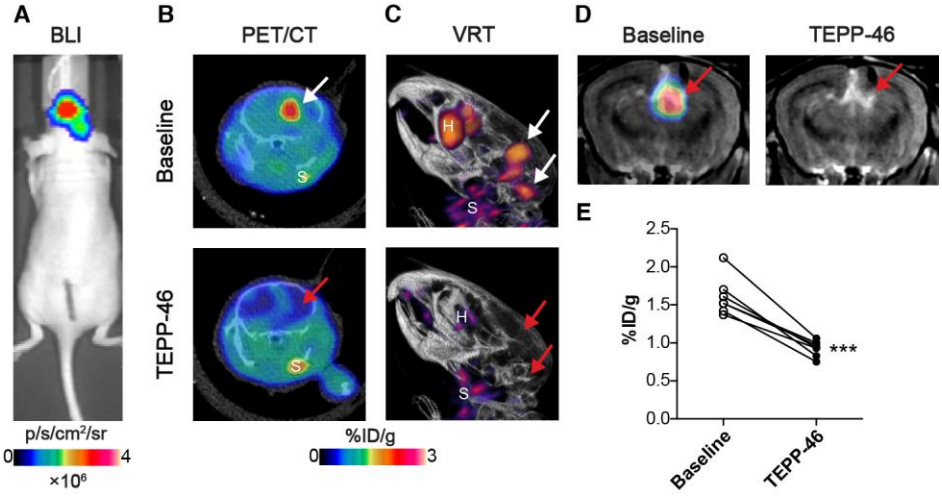

Fig. 6. Assessment of TEPP-46 binding efficacy with [^{11}C]DASA-23 in orthotopic GBM39 PDX tumors. (**A**) Bioluminescence imaging of an orthotopically-implanted GBM39 tumor 50 days after injection. (**B**) [^{11}C]DASA-23 PET/CT (10 – 30 min summed activity) images of the head of a GBM39 tumor-bearing mouse at baseline, reimaged the following day 1 hour after TEPP-46 injection (50 mg/kg i.p.). Arrows indicate the location of the tumor. (**C**) 3D VRT images of the same animal. Arrows indicate the location of the tumor. H, harderian glands; S, salivary glands. (**D**) Merged [^{11}C]DASA-23-PET/MR images (10 – 30 min summed [^{11}C]DASA-23 activity) at baseline and after TEPP-46 injection. Arrows indicate the location of the tumor. (**E**) Semi-quantitative uptake values in GBM39 tumors before and after TEPP-46 blocking, taken 30 min after [^{11}C]DASA-23 injection. Data shown as mean ± SD (n = 7 animals). BLI, bioluminescence imaging; T_1W-MRI, T_1-weighted nuclear magnetic resonance imaging; NS, not significant; VRT, volume rendering technique. ***, $P < 0.001$.